Asymmetric Rotor Design of IPMSM for Vibration Reduction Under Certain Load Condition

Young-Hoon Jung, Min-Ro Park, and Myung-Seop Lim, *Member, IEEE*

***Abstract*—This paper proposes the design method using a numerical formula known as the Advanced Inverse Cosine Function (AICF) to reduce vibration of the Interior Permanent Magnet Synchronous Motor (IPMSM). The proposed method reduces the vibration by modifying the rotor shape based on the numerical formula that makes the air-gap flux density sinusoidal under certain load condition. The radial electromagnetic force that is the source causing the vibration of the motor is related to the air-gap flux density under load condition. Therefore, the AICF which reduces the magnitude of the harmonic of the air-gap flux density is derived in this paper and the radial electromagnetic force due to the harmonic of the air-gap flux density decreases applying the AICF. To verify the validity of the proposed method, an 8 pole 12 slot prototype applied with the AICF is proposed. Using the Finite Element Analysis (FEA), the radial electromagnetic force and the displacement of the prototype with the AICF are compared with those of the normal model without the AICF. Finally, the results of the vibration test of the normal and AICF models are compared.**

***Index Terms*—Advanced inverse cosine function (AICF), asymmetric rotor shape, concentrated flux-type synchronous motor (CFSM), displacement, interior permanent magnet synchronous motor (IPMSM), radial electromagnetic force, vibration.**

I. Introduction

IN RECENT years, electric motors have been used in various fields such as automobiles and home appliances, and the use of these electric motors is increasing [1]. More specifically, applications such as automobiles and home appliances require high efficiency and high power density. The Interior Permanent Magnet Synchronous Motors (IPMSM) with a permanent magnet (PM) embedded in the rotor is the most attractive motor to satisfy these characteristics among the various types of electric motors. This is because the IPMSM can use not only magnetic torque but also reluctance torque due to the difference in inductance magnitude between the *d*-axis and *q*-axis. However, since these applications are closely related to daily life, consumer demand for noise and vibration reduction of these applications is increasing and many related studies are being carried out.

Manuscript received August 2, 2019; revised November 19, 2019; accepted January 8, 2020. Date of publication January 13, 2020; date of current version May 20, 2020. This work was supported by the National Research Foundation of Korea Grant funded by the Korea government (MSIP; Ministry of Science, ICT & Future Planning) under Grant 2018R1C1B5085447. Paper no.-TEC-00806-2019 *(Corresponding author: Myung-Seop Lim.)*

The authors are with the Department of Automotive Engineering, Hanyang University, Seoul 04763, Korea (e-mail: yhjung207@hanyang.ac.kr; minro1226@hanyang.ac.kr; myungseop@hanyang.ac.kr).

Color versions of one or more of the figures in this article are available online at https://ieeexplore.ieee.org.

Digital Object Identifier 10.1109/TEC.2020.2966299

The radial electromagnetic force is one of the main causes of the noise and vibration of the motor. The sources of the radial electromagnetic force are divided into two categories: magnetic, and electronic sources [2]. The noise and vibration due to the electronic source of the radial electromagnetic force are produced by input included the harmonics because the radial electromagnetic forces due to the harmonics input are additionally generated. In [3]–[7], the research has been studied from the control point of view to reduce the electronic source. The vibration and noise caused by the magnetic source are generated when the radial electromagnetic force in the air-gap is applied to the stator and the stator is deformed.

Much of the research on the noise and vibration has been studied from the design point of view to reduce the radial electromagnetic force due to the magnetic source. In [8]–[13], studies on the effect of the number of poles and slots on the vibration are investigated by changing the number of poles and slots. Reference [8] studied the effect of the unbalanced radial electromagnetic force on the vibration and noise on the electric motor for 8 poles 9 slots and 8 poles 12 slots. In [9], the tendency of the vibration is investigated by changing the pole and slot combination; 8 poles 48 slots, 8 poles 72 slots, 46 poles 48 slots, and 50 poles 48 slots. In [10], the noise and vibration characteristics of two concentrated windings are compared. Reference [11] investigated the radial electromagnetic force and vibration order of the various fractional slot machines, where the vibration order represents a spatial distribution of the radial electromagnetic force at a specific time. Reference [12], [13] proposed the method of selecting the number of poles and slots using the vibration order to reduce the vibration. This is because the displacement that occurs during the vibration is inversely proportional to the fourth order of vibration order [14]. However, changing the number of poles and slots for vibration reduction is the inconvenient because it requires the redesigning of the electric motor and altering of the control characteristics due to changes in carrier frequency.

In [15]–[24], the research on noise and vibration according to the modified shape of the designed motor was conducted. In [15], [16], the vibration is reduced by changing the pole angle. In [16], the length of the PM, the length of the tooth, and the thickness of the tooth shoe are additionally optimized to reduce the vibration. Reference [17] researched the tendency of the vibration on various yoke and tooth shapes and presented an improved model. In [18], the slotting effect on the radial electromagnetic force is researched and the slot opening width is optimized to reduce the radial electromagnetic force. Reference [19], [20]

applies the notch to the rotor for the vibration reduction. In [19], the chamfer to the stator is also applied to decrease the vibration. In [21], the vibration is reduced by optimizing the stator shape. In [22]–[24], skew is applied to the rotor or stator to decrease the vibration. These researches reduce the vibration through modification of the air-gap flux density because the radial electromagnetic force is proportional to the square of the air-gap flux density. However, since the method of modifying the shape of the designed motor for vibration reduction mainly uses the optimization techniques, these methods require many analysis results and are time consuming.

This paper proposes the method of the vibration reduction by changing the rotor shape to make the air-gap flux density sinusoidal under the certain load condition. Previous studies reduced the vibration by changing the shape of the motor using the optimization technique. However, the proposed method in this paper is the method of making the air-gap flux density sinusoidal by using the numerical formula without using the optimization technique. The numerical formula used in this paper is called the Advanced Inverse Cosine Function (AICF) which is derived from the Inverse Cosine Function (ICF) [25]. Unlike the ICF, the AICF is considered the magnetic field by the armature reaction as well as that of the PM. Therefore, when the AICF is applied, the asymmetric rotor shape is obtained because the armature reaction is considered. In [25], the torque ripple is reduced by applying the AICF which makes the air-gap flux density under the load condition sinusoidal. Also, as with the torque ripple, the radial electromagnetic force that causes the vibration of the motor is related to the air-gap flux density under the load condition. Thus, this paper proposes the method to reduce vibration by applying the AICF. By applying the AICF, the radial electromagnetic force due to the harmonic component of the air-gap flux density of the AICF model is reduced than that of the normal model. Therefore, the displacement causing the vibration of the AICF model is reduced compared with that of the normal model with the cylindrical rotor without the AICF applied. To verify the vibration reduction of the proposed method, the radial electromagnetic force and the displacement of the AICF model are compared with those of the normal model using a finite element analysis (FEA) in this paper. Finally, the AICF model and normal model are manufactured and tested under the rated load condition, and the test result of the AICF model is compared with that of the normal model.

II. Relationship Between Electromagnetic Force and Air-Gap Flux Density

The radial electromagnetic force generated in the element of the air-gap is represented by (1), which is the product of the radial electromagnetic force density and the cross-sectional area of the element of the air-gap.

$$F_r = P_r A_e = P_r r_g \theta_e L_{stk} \tag{1}$$

where, F_r is the radial electromagnetic force; P_r is the radial electromagnetic force density; A_e is the cross-sectional area of the element in which the radial electromagnetic force is generated; r_g is the radius of the air-gap; θ_e is the angle between nodes of the element; and L_{stk} is the stack length of the motor. If the tangential air-gap flux density is ignored for the convenience of the analytical approach, the radial electromagnetic force density and the radial air-gap flux density have the relationship of (2) by the Maxwell stress tensor method.

$$P_r = \frac{B_{g,r}^2 - B_{g,t}^2}{2\mu_0} \approx \frac{B_{g,r}^2}{2\mu_0} \tag{2}$$

where $B_{g,r}$ is the radial air-gap flux density; $B_{g,t}$ is the tangential air-gap flux density; and μ_0 is the permeability in vacuum.

The radial air-gap flux density is composed of the magnetic field by the PM and the armature reaction. In the case of a motor with a tooth and slot structure, the tooth and slot structure affect the air-gap magnetic field. To reflect this effect in a smooth air-gap, the relative specific permeance is considered in the air-gap magnetic distribution. Thus, the radial air-gap flux density, considering the tooth and slot structure, is expressed as (3).

$$B_{g,r} = (B_{g,m} + B_{g,a})\,\Lambda_a \tag{3}$$

where $B_{g,m}$ is the radial flux density by the PM; $B_{g,a}$ is the radial flux density by the armature reaction; and Λ_a is the relative specific permeance.

Equation (3) is substituted into (2), and (4) is obtained. As shown in (4), the radial electromagnetic force density is affected by the resultant air-gap flux density which is the sum of the magnetic flux density due to the PM and the armature reaction.

$$P_r = \frac{(B_{g,m} + B_{g,a})^2 \Lambda_a^2}{2\mu_0} \tag{4}$$

The harmonics of the resultant air-gap flux density generates the radial electromagnetic force with the various time harmonic and vibration order [12], [13]. Especially, some harmonics of the resultant air-gap flux density generate the radial electromagnetic forces with the low vibration order. Since the relationship between the vibration order and the displacement causing the vibration is expressed as (5), the radial electromagnetic forces with the low vibration order have a great effect on the vibration.

$$\Delta d \propto \frac{1}{r^4} \tag{5}$$

where, Δd is the displacement; and r is the vibration order. Therefore, to reduce the vibration, the radial electromagnetic forces with the low vibration order should decrease. As a result, it is necessary to make the resultant air-gap flux density sinusoidal.

III. Asymmetric Rotor Shape for Harmonic Reduction of Resultant Air-Gap Flux Density

There are various methods for harmonic reduction of the air-gap flux density. Among the various methods, the eccentric rotor shape or the Inverse Cosine Function (ICF) are generally used to reduce harmonic of the air-gap flux density. The rotor shapes applying the eccentric rotor shape and ICF are shown in Fig. 1. As shown in Fig. 1, these two methods have the smallest air-gap length in the *d*-axis and increase the air-gap length toward the *q*-axis. Both methods also have symmetrical air-gap length along the d-axis. These methods make the air-gap flux density sinusoidal under the no-load condition [25]. However, as

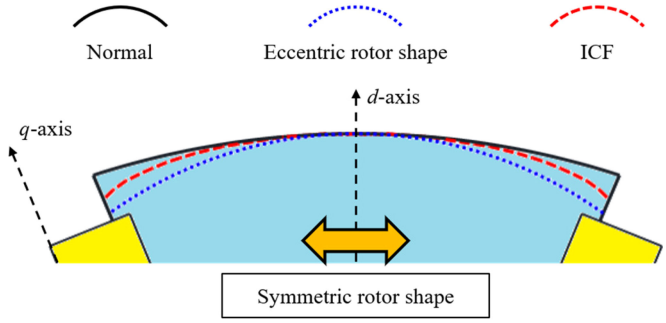

Fig. 1. Rotor shape comparison of the normal, eccentric rotor shape, and ICF model.

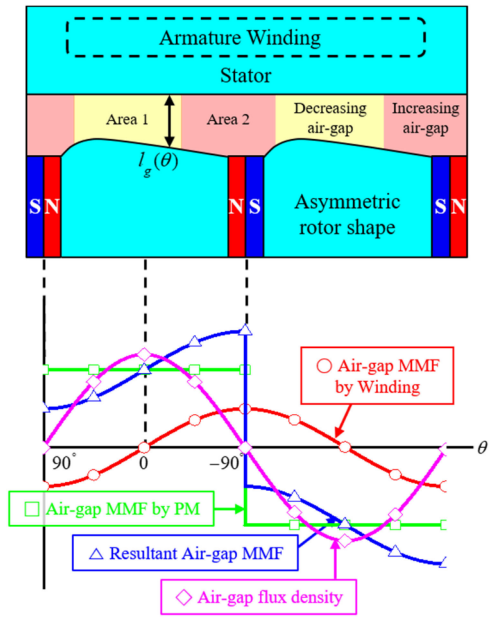

Fig. 2. Air-gap MMF distribution and flux density under the load condition.

mentioned earlier, the air-gap flux density on the load condition must be made sinusoidal to reduce the vibration of the motor. This paper proposes the Advanced Inverse Cosine Function (AICF) which is a function that determines the air-gap length to make the air-gap flux density sinusoidal under the certain load condition.

A. Advanced Inverse Cosine Function: AICF

As previously mentioned, the AICF makes the air-gap flux density sinusoidal on the load condition. The distribution of the magneto motive force (MMF) in the PM (Green square symbol in Fig. 2) and the armature reaction (Red circle symbol in Fig. 2) under the load condition is shown in Fig. 2. As shown in Fig. 2, the air-gap MMF by the PM is considered a square wave, and the air-gap MMF by armature reaction is considered only the fundamental component. The resultant air-gap MMF (Blue triangle symbol in Fig. 2) is the sum of the MMF by the PM and the armature reaction and is expressed as (6).

$$F_g = F_m - F_a \sin(\theta + \beta) \tag{6}$$

where F_g is the resultant air-gap MMF; F_m is the air-gap MMF by the PM; F_a is the air-gap MMF by the armature reaction; θ is the electrical angle; β is the current phase angle.

The relation between the resultant air-gap MMF and the radial air-gap flux density is shown in (7).

$$B_{g,r} = \frac{\mu_0 F_g}{l_g} = \frac{\mu_0 \{F_m - F_a \sin(\theta + \beta)\}}{l_g} \tag{7}$$

where l_g is the air-gap length. As seen in (7), to make the radial air-gap flux density sinusoidal (Pink diamond symbol in Fig. 2), the air-gap length should be adjusted appropriately. The sinusoidal air-gap flux density can be expressed as (8), according to the angle, θ. The range of θ is from $-90^\circ \sim 90^\circ$ in the electrical angle.

$$B_{\max} \cos\theta = \frac{\mu_0 \{F_m - F_a \sin(\theta + \beta)\}}{l_g(\theta)} \tag{8}$$

where $B_{\max}$ is the maximum value of the air gap flux density and $l_g(\theta)$ is the air gap length according to θ.

Therefore, the function determining air-gap length to make the air-gap flux density sinusoidal is expressed as (9). Equation (9) is called as the Advanced Inverse Cosine Function (AICF).

$$l_g(\theta) = \frac{l_d}{\cos\theta} - k_F \frac{l_d \sin(\theta + \beta)}{\cos\theta} \tag{9}$$

where l_d is the d-axis air-gap length; k_F is the MMF ratio; l_d and k_F are expressed as (10) and (11), respectively.

$$l_d = \frac{\mu_0 F_m}{B_{\max}} \tag{10}$$

$$k_F = \frac{F_a}{F_m} \tag{11}$$

To calculate k_F, the air-gap MMFs by the PM and the armature reaction should be calculated. The air-gap MMFs by the PM and the armature reaction are calculated by using (12) and (13), respectively.

$$F_m = \frac{B_r A_m l_m l_g}{\mu_0 (\mu_{rec} A_m l_g + A_g l_m)} \tag{12}$$

$$F_a = 1.5 k_w \frac{\sqrt{2} N_{ph} I_{rms}}{2p} \tag{13}$$

where B_r is the residual induction of the PM; A_m is the cross-sectional area of the PM; l_m is the thickness of the PM; μ_{rec} is the recoil permeability of the PM; A_g is the cross-sectional area of the air-gap; k_w is the winding factor; N_{ph} is the number of the series turns per phase; I_{rms} is the rms value of the current; and p is the number of pole pairs.

According to (9), the area 1 in the air-gap between the simplified rotor and stator of Fig. 2 is the area in which the air-gap length is shorter than the d-axis air-gap length, and the area 2 of Fig. 2 is the area that is larger than the d-axis air-gap length. The areas of 1 and 2 differ on k_F and β.

B. Offset δ for Mechanical Clearance

If the air-gap length is calculated using (9), the air-gap length less than the air-gap length of the normal model is calculated

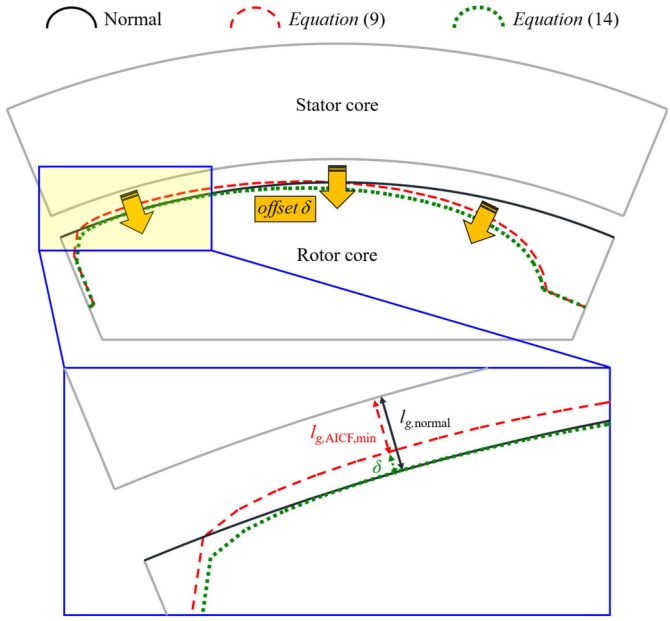

Fig. 3. Rotor shape considering δ offset.

according to the position. Because the minimum air-gap length is selected considering the mechanical stability and manufacturing tolerance, the minimum air-gap length of the AICF should be the same length as that of the normal model. Therefore, the AICF is modified as (14) to have the same air-gap length as the normal model. The added air-gap length, δ is calculated by (15).

$$l_g(\theta) = \frac{l_d}{\cos\theta} - k_F \frac{l_d \sin(\theta+\beta)}{\cos\theta} + \delta \tag{14}$$

$$\delta = l_{g,\mathrm{normal}} - l_{g,\mathrm{AICF,min}} \tag{15}$$

where $l_{g,\mathrm{normal}}$ is the air-gap length of the normal model; and $l_{g,\mathrm{AICF,min}}$ is the minimum air-gap length of the AICF model. Fig. 3 shows the difference of the rotor shapes among the normal model and the AICF models using (9) and (14). To verify the effectiveness of the proposed method, the vibration characteristics of the normal model and the AICF model are compared using FEA in the next section.

IV. Comparison of Vibration Characteristics Using FEA

The vibration characteristic of the AICF is compared with that of the normal model. The process of the vibration analysis is shown in Fig. 4. First, the radial and tangential air-gap flux density of the analysis model is calculated for time and space using the two-dimensional (2D) electro-magnetic field FEA. The 2D electro-magnetic field FEA conducted in this paper is nonlinear analysis considering the magnetic saturation of the core. A transient analysis is conducted, and the input current is assumed to be an ideal sine wave able to ignore the effect of the pulse width modulation (PWM). Secondly, the radial electromagnetic force of the analysis model is calculated from the radial and tangential air-gap flux density using (1) and (2). Next, the radial electromagnetic force is divided into the time

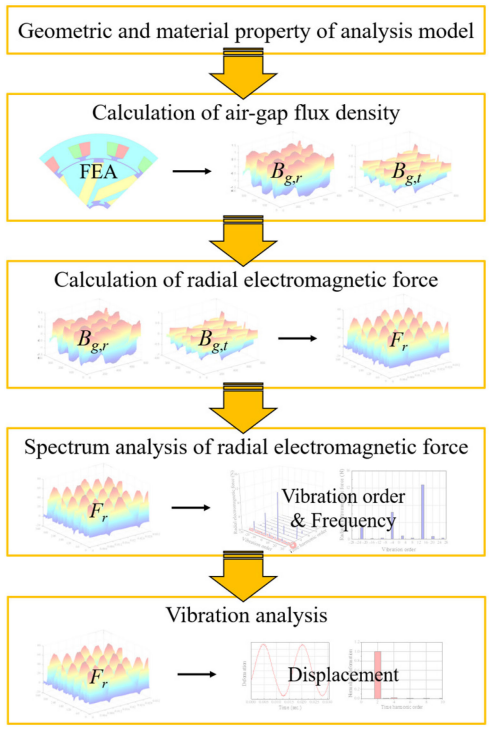

Fig. 4. Process of the vibration analysis.

harmonic and the spatial harmonic to confirm the harmonics of the radial electromagnetic force through the spectrum analysis. Finally, the vibration analysis is conducted to calculate the displacement of the stator applied the radial electromagnetic force using the mechanical field FEA. The displacement of the stator is calculated using the mode superposition method.

The two vibration characteristics of the normal model and the AICF model are compared through the vibration analysis. First, the radial electromagnetic forces of the AICF model and the normal model are compared because the radial electromagnetic force generates the vibration of the motor. Secondly, the stator displacement generated from the radial electromagnetic force of the both models is compared.

A. Model Information

In this paper, the normal and AICF models are proposed. All the proposed models are spoke type IPMSMs with PMs arranged diagonally to increase the air-gap flux density at the same outer diameter of the rotor. The stator of the AICF model is used as the same stator of the normal model. The model specification is summarized in Table I. Fig. 5 shows the configuration of the proposed models. To compare the differences in the rotor shape, the overlapped rotor shape of the proposed models is shown in Fig. 6. As shown in Fig. 6, the air-gap length of the AICF model is asymmetric, unlike the normal model, because the armature reaction is considered. Fig. 7 shows the torque waveforms under the rated load condition (30 $\mathrm{A_{rms}}$, 0°) of the two models obtained from the FEA. As shown in Fig. 7, the average torque of the AICF model is similar to that of the normal model, but the torque ripple of the AICF model is much lower than that of the normal model.

TABLE I
MODEL SPECIFICATION

Quantity	Unit	Value
Pole / slot number	-	8 / 12
Rotor Outer diameter	mm	119
Stator inner diameter	mm	120.7
Stator Outer diameter	mm	170
Stack length	mm	135
Core material	-	50PN470
Residual induction	T	0.38
Rated speed	rpm	2000
Rated torque	Nm	24
Rated current	A_{rms}	30
Rated Power	kW	5
Drive method	-	I_d=0 control
k_F	-	0.80
δ	mm	0.34

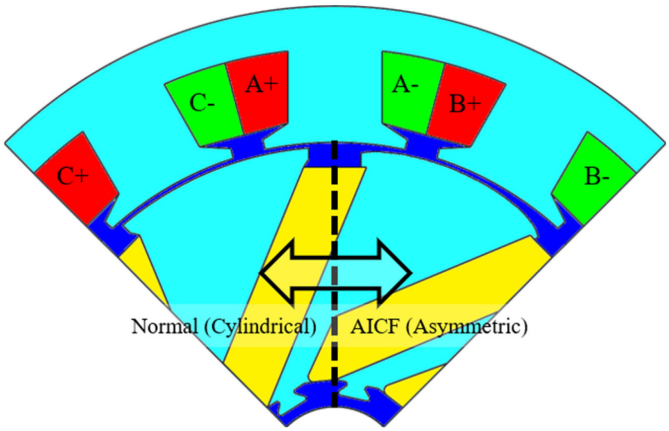

Fig. 5. Configuration of the proposed models.

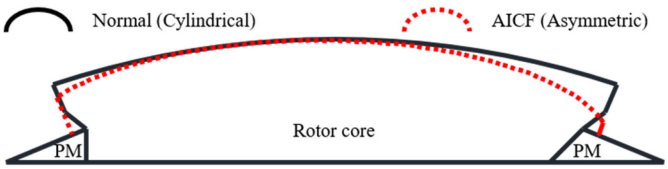

Fig. 6. Overlapped rotor shape of the proposed models.

This is because the air-gap flux density of the AICF model is more sinusoidal than that of the normal model. The comparison of the air-gap flux density waveforms of the two models is shown in the next section.

B. Comparison of Radial Electromagnetic Force

The radial electromagnetic force of the normal model and the AICF model is calculated using a nonlinear FEA. Using the nonlinear FEA, the radial and tangential flux density of the air-gap are calculated for time and space. The electro-magnetic

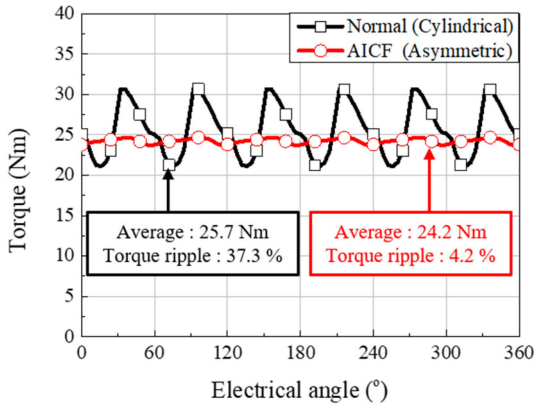

Fig. 7. Torque waveform of the two models obtained from FEA.

analysis is conducted on the rated current condition, 30 A_{rms} and 0°. The analysis time is an electrical one period and the air-gap flux density is calculated mechanically for 360°. The air-gap flux density waveforms of the normal and AICF models under the rated load condition is seen in Fig. 8(a) and (b), respectively. As shown in Fig. 8(a) and (b), the air-gap flux density of the AICF model is more sinusoidal than that of the normal model. Since the AICF is derived to make the spatial distribution of the air-gap flux density sinusoidal, the spatial distributions of the air-gap flux density of the two models at 0 sec., indicated by red lines in Fig. 8(a) and (b), are shown in Fig. 8(c). As shown in Fig. 8(c), the air-gap flux density of the AICF model becomes lower in the region where the normal model shows a high flux density. On the other hand, in the region where the flux density of the normal model is low, the air-gap flux density of the AICF model is higher. Therefore, the air-gap flux density of the AICF model becomes more sinusoidal. In Fig. 8(c), the total harmonic distortions of the normal and AICF models are 56.86% and 44.49%, respectively, indicating that the harmonics of the AICF model are lower than those of the normal model. This is because the air-gap length is adjusted using (14) so that the air-gap flux density becomes sinusoidal.

The radial electromagnetic force is calculated from the radial and tangential air-gap flux density using (1) and (2). The radial electromagnetic force is also a function of time and space, because the radial and tangential air-gap flux density is a function of time and space. The radial electromagnetic force according to the time and space in the mechanical angle of the AICF and normal model is seen in Fig. 9(a) and (b). As shown in Fig. 9(a) and (b), the radial electromagnetic force waveform of the AICF model contains less harmonics than that of the normal model. Fig. 9(c) shows the spatial distribution of the radial electromagnetic force of the two models, indicated by the red lines in Fig. 9(a) and (b). Since the air-gap flux density of the AICF model is more sinusoidal than that of the normal model, the radial electromagnetic force of the AICF model has fewer harmonics and smaller magnitude than that of the normal model, as shown in Fig. 9(c). To confirm the fact that the radial electromagnetic force of the AICF model contains less harmonics compared with that of the normal model, the radial

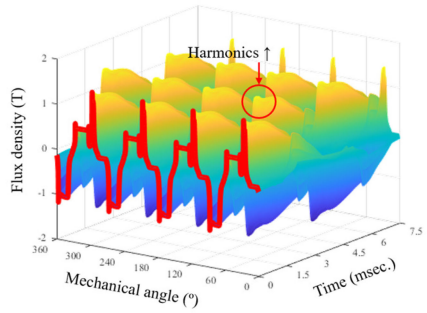

(a)

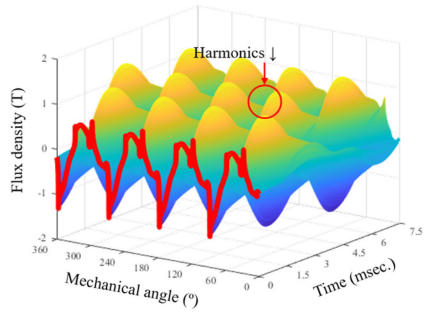

(b)

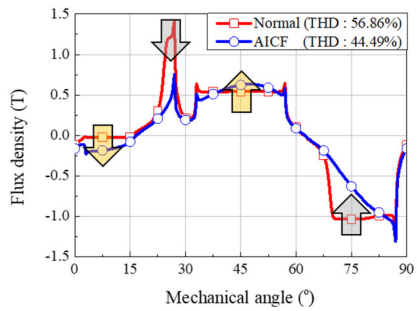

(c)

Fig. 8. Air-gap flux density waveforms under the rated load condition. (a) Normal (Cylindrical). (b) AICF (Asymmetric). (c) Comparison of the spatial distribution of air-gap flux density between the two models at 0 sec.

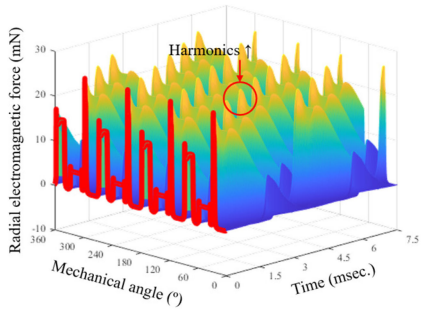

(a)

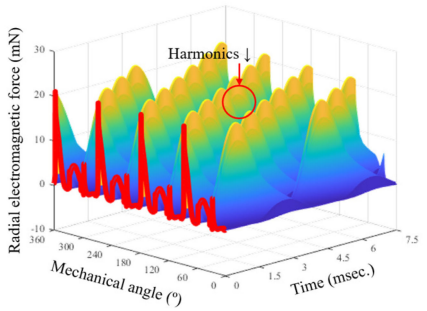

(b)

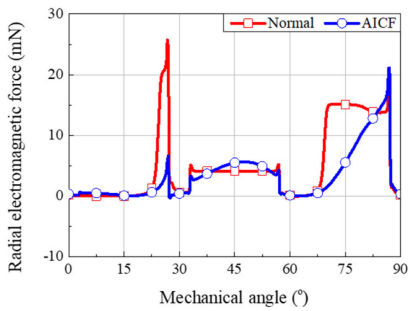

(c)

Fig. 9. Radial electromagnetic force. (a) Normal (Cylindrical). (b) AICF (Asymmetric). (c) Comparison of the spatial distribution of the radial electromagnetic force between the two models at 0 sec.

electromagnetic force is divided into the time and vibration order through the spectrum analysis. The vibration order represents the spatial distribution of the radial electromagnetic force. The results of the spectrum analysis of the two models under the rated load condition are shown in Fig. 10. The frequency of the radial electromagnetic force is an even multiple of the line frequency f which is the frequency of the input current. The vibration order of the radial electromagnetic force generated at each frequency is obtained as shown in Table II [12], [13]. In Table II, μ and ν are the spatial harmonic order of the air-gap MMF by the field and armature reaction, respectively; s and k are the number of slots and natural numbers, respectively. As shown in Fig. 10, the radial electromagnetic force of all time harmonic order of the AICF model is reduced more than that of the normal model. In particular, the decrease in the radial electromagnetic force of the time harmonics above the fourth order or more of the AICF model is remarkable. Thus, the vibration due to the radial electromagnetic force of the time harmonics above the fourth order or more of the AICF model is smaller than that of the normal model.

According to (5), The vibration of the motor is affected not only by the magnitude of the radial electromagnetic force, but also by the vibration order of the radial electromagnetic force. In the second order time harmonic, the lowest vibration order is 4. The radial electromagnetic force with the vibration order of 4 has a smaller radial electromagnetic force than that with the vibration order of 8 but has a greater effect on the vibration than that with the vibration order of 8 by (5). As shown in Table II,

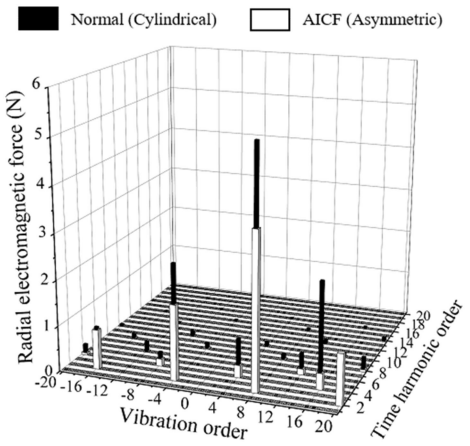

Fig. 10. Spectrum analysis result of the radial electromagnetic force under the rated load condition.

TABLE II
[12], [13] VIBRATION ORDER AND FREQUENCY OF RADIAL ELECTROMAGNETIC FORCE

Contents	Vibration order	Frequency
Self of PM fields	$p(\mu_1 \pm \mu_2)$	$(\mu_1 \pm \mu_2)f$
Self of armature reaction fields	$p(\nu_1 \pm \nu_2)$	$(n_1 \pm n_2)f$
Interaction of the PM and armature reaction fields	$p(\mu \pm \nu)$	$(\mu \pm n)f$
Interaction of the PM field and stator slotting	$p(\mu_1 \pm \mu_2) \pm ks$ or $p(\mu_1 \pm \mu_2) \pm (k_1 \pm k_2)s$	$(\mu_1 \pm \mu_2)f$
Interaction of the armature reaction field and stator slotting	$p(\nu_1 \pm \nu_2) \pm ks$ or $p(\nu_1 \pm \nu_2) \pm (k_1 \pm k_2)s$	$(n_1 \pm n_2)f$

because the radial electromagnetic force with the vibration order of 4 is generated from the interaction of harmonics of the PM and armature reaction fields, the magnitude of the radial electromagnetic force with the vibration order of 4 of the AICF model is smaller than that of the normal model. Therefore, the vibration of the second order time harmonic, which is the largest component in the vibration of the motor, is reduced.

Additionally, comparisons of the radial electromagnetic force under load conditions other than the rated load condition are shown in Fig. 11. The load conditions examined are 30 A_{rms}, 30° and 30 A_{rms}, 60°. As shown in Fig. 11, the radial electromagnetic forces of the AICF model are smaller than those of the normal model, under both conditions. It can be concluded that the vibration of the AICF model is also reduced than that of the normal model under load conditions other than the rated load condition to which the AICF was applied. In the next section, the vibration analysis is performed only for the rated condition.

C. Comparison of Displacement

The vibration analysis is conducted using Ansys Mechanical APDL. The displacement of the stator is calculated using the mode superposition method and the previously calculated radial

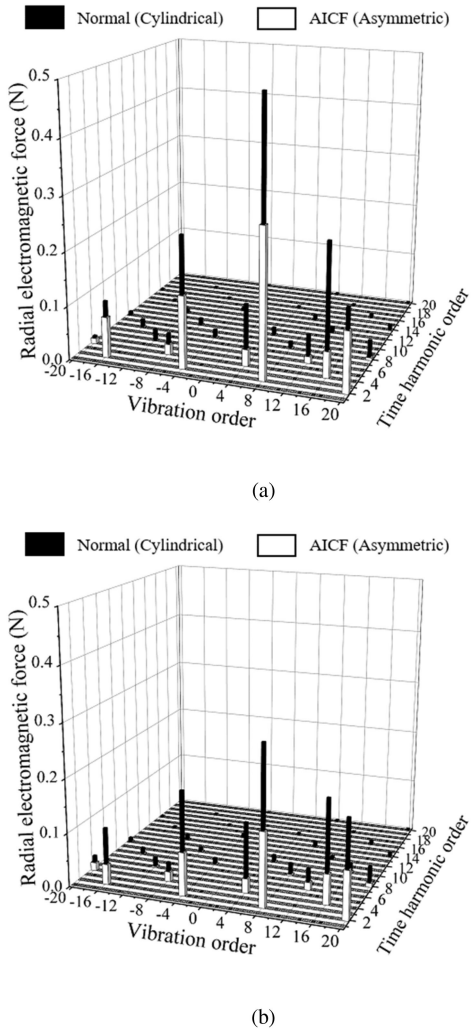

Fig. 11. Spectrum analysis result of two other conditions. (a) 30 A_{rms}, 30°. (b) 30 A_{rms}, 60°.

electromagnetic force under the rated load condition. The previously calculated radial electromagnetic force is applied to each node of the inner surface of the stator as the nodal force. In the mechanical field FEA, the governing equation to calculate the displacement of the stator is expressed as (16). The displacement with respect to the time is calculated considering the spatial distribution of the radial electromagnetic force [12], [13].

$$[M]\sum_{i=1}^{N}\{\Phi_i\}\,\ddot{y}_i + [C]\sum_{i=1}^{N}\{\Phi_i\}\,\dot{y}_i + [K]\sum_{i=1}^{N}\{\Phi_i\}\,y_i = \{F\} \tag{16}$$

where, $[M]$ is the matrix of mass; N is the number of modes to be summed; $\{\Phi_i\}$ is the modal shape of mode i; y_i is nodal displacement in modal coordinates; $[C]$ is the matrix of damping; $[K]$ is the matrix of stiffness; $[M]$, $[C]$, and $[K]$ are calculated for each element via the mechanical field FEA using the material properties and shape of the stator. $\{F\}$ is the radial electromagnetic nodal force varying in time.

The harmonic analysis of the displacement with respect to the time calculated using (16) is performed. The results of

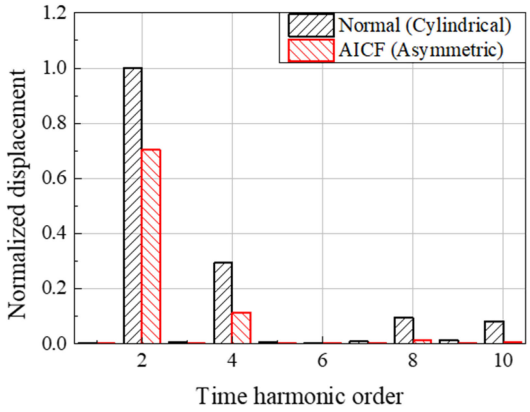

Fig. 12. Harmonic analysis result of displacement according to the models under the rated load condition.

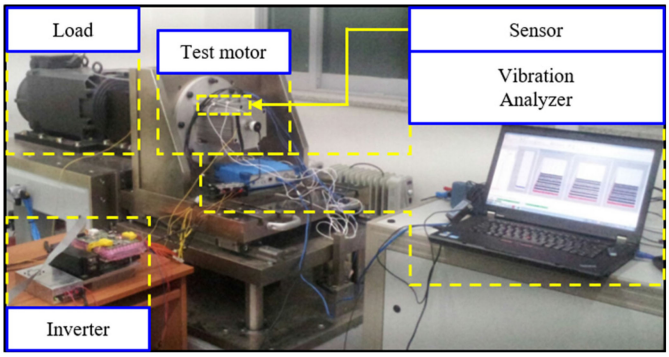

Fig. 13. Experimental setup.

the harmonic analysis of the displacement of the AICF model and normal model under the rated load condition are shown in Fig. 12. The frequency at which displacement occurs is also equal to the frequency of the radial electromagnetic force ($2nf$, $n = 1, 2, 3, \ldots$). As shown in Fig. 12, at all frequencies, the displacement of the AICF model is less than the displacement of the normal model. This is because the space and time harmonic components of the radial electromagnetic force of the AICF model are reduced compared to that of the normal model under the same stator condition, as shown in Fig. 10.

V. Validation

In order to validate the vibration reduction of the proposed method, the experiment is conducted at the rated load condition, 30 A_{rms}, 0°, and 2000 rpm. During the test, the test motor is connected in series with the torque sensor and the load, mechanically. The induction motor of 50 kW is used for the load and the 4503A type of KISTLER is used as the torque sensor. The OR35 Modular Analyzer of OROS is used for the vibration measurement. The sensor is attached to the motor housing surface. Figs. 13 and 14 show the experimental setup and the manufactured motors which are the normal model and the AICF model, respectively. The experimental results of the torque and vibration are shown in Fig. 15. Fig. 15(a) shows the experimental torque waveform under the rated load condition. Also, the numerical values for the average torque and torque

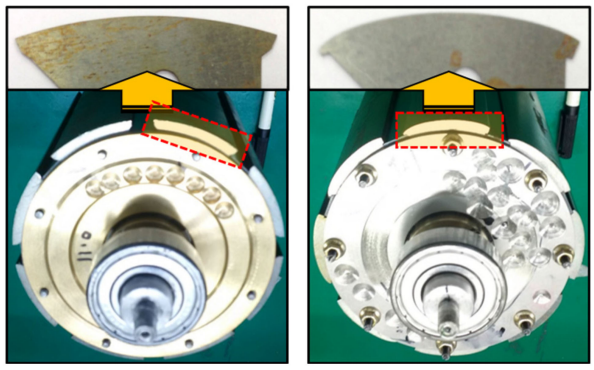

(a) (b)

Fig. 14. Manufactured rotors and samples. (a) Normal (Cylindrical). (b) AICF (Asymmetric).

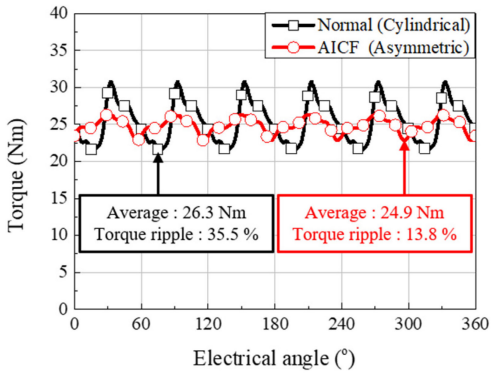

(a)

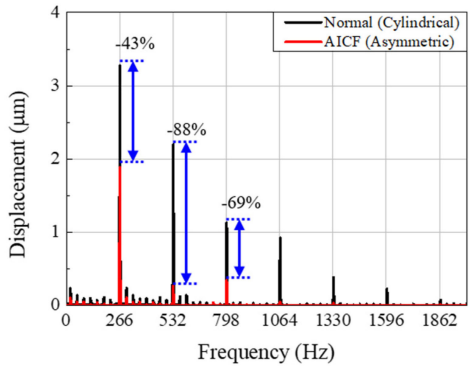

(b)

Fig. 15. Experimental result. (a) Torque. (b) Vibration.

ripple of the two models are specified in Fig. 15(a). Like the FEA result in Fig. 7, the average torque of the AICF model is similar to that of the normal model, but the torque ripple of the AICF model is lower at 21.7% than that of the normal model. The experimental result of vibration is shown in Fig. 15(b). As shown in Fig. 15(b), the vibration occurred at the same frequency as the vibration analysis. The displacement of the AICF model is smaller than that of the normal model at all frequencies, which is the same result as the vibration analysis. In particular, the displacement of the normal model occurs above

1000 Hz, while there is little displacement of the AICF model. The displacement of the AICF model at the 2*f*, 4*f* and 6*f* is reduced by 43%, 88% and 69% compared to those of the normal model, respectively. The tendency of the displacement of the AICF model to be reduced compared to the normal model is the same as the simulation result in Fig. 12. Therefore, it can be concluded that the model applying the proposed method in this paper is effective for vibration reduction.

VI. Conclusion

This paper proposes the asymmetric rotor shape design using the AICF to reduce the vibration. Because the vibration is caused by the radial electromagnetic force, the magnitude of the radial electromagnetic force needs to be reduced. More specifically, the radial electromagnetic forces with a low vibration order have a great effect on the vibration, and these forces generate from the harmonics of the resultant air-gap flux density. Therefore, the AICF that makes the resultant air-gap flux density sinusoidal is derived and, by applying the AICF, the magnitude of the radial electromagnetic force due to the harmonics of the air-gap flux density is reduced. This is confirmed by the electro-magnetic field FEA and spectrum analysis of the radial electromagnetic force. As a result of the spectrum analysis, the magnitude of the radial electromagnetic force due to the time and space harmonics of the air-gap flux density of the AICF model is smaller than that of the normal model. The result of the vibration analysis of the AICF model also decreased compared to that of the normal model because the magnitude of the radial electromagnetic force of the AICF model was reduced compared to that of the normal model. To verify the effect of the vibration reduction of the proposed method, the test was conducted under the rated load condition, 30 A_{rms}, 0°, and 2000 rpm. The test results have the same tendency as the vibration analysis. In the test results, the displacement of the normal model occurred above 1000 Hz, but the displacement of the AICF model was little. Moreover, in the case of 2*f*, 4*f* and 6*f*, the AICF model decreased by 43%, 88% and 69% compared with the normal model, respectively. Therefore, it is concluded that the proposed method is effective for the vibration reduction.

References

[1] M.-R. Park, H.-J. Kim, Y.-Y. Choi, J.-P. Hong, and J.-J. Lee, "Characteristics of IPMSM according to rotor design considering nonlinearity of permanent magnet," *IEEE, Trans. Magn.*, vol. 52, no. 3, Mar. 2016, Art. no. 8101904.

[2] P. Vijayraghavan and R. Krishnan, "Noise in electric machines: A review," *IEEE Trans. Ind. Appl.*, vol. 35, no. 5, pp. 1007–1013, Sep./Oct. 1999.

[3] X. Han, D. Jiang, T. Zou, R. Qu, and K. Yang, "Two-segment three-phase PMSM drive with carrier phase-shift PWM for torque ripple and vibration reduction," *IEEE Trans. Power Electron.*, vol. 34, no. 1, pp. 588–599, Jan. 2019.

[4] D. Torregrossa, D. Paire, F. Peyraut, B. Fahimi, and A. Miraoui, "Active mitigation of electromagnetic vibration radiated by PMSM in fractional-horsepower drives by optimal choice of the carrier frequency," *IEEE Trans. Ind. Electron.*, vol. 59, no. 3, pp. 1346–1354, Mar. 2012.

[5] Y. Miyama, H. Kometani, and K. Akatsu, "Vibration reduction by applying carrier phase-shift PWM on dual three-phase winding permanent magnet synchronous motor," *IEEE Trans. Ind. Appl.*, vol. 54, no. 6, pp. 5998–6004, Nov. 2018.

[6] C. Gan, J. Wu, Q. Sun, W. Kong, H. Li, and Y. Hu, "A review on machine topologies and control techniques for low-noise switched reluctance motors in electric vehicle applications," *IEEE Access*, vol. 6, pp. 31430–31443, 2018.

[7] R. Zhong, X. Guo, M. Zhang, D. Ding, and W. Sun, "Influence of switch angles on second-order current harmonic and resonance in switched reluctance motors," *IET Electr. Power Appl.*, vol. 12, no. 9, pp. 1247–1255, 2018.

[8] T. Sun, J.-M. Kim, G.-H. Lee, J.-P. Hong, and M.-R. Choi, "Effect of pole and slot combination on noise and vibration in permanent magnet synchronous motor," *IEEE Trans. Magn.*, vol. 47, no. 5, pp. 1038–1041, May. 2011.

[9] G. Verez, G. Barakat, Y. Amara, and G. Hoblos, "Impact of pole and slot combination on vibrations and noise of electromagnetic origins in permanent magnet synchronous motors," *IEEE Trans. Magn.*, vol. 51, no. 3, Mar. 2015, Art. no. 8101104.

[10] G. Dajaku, H. Hofmann, F. Hetemi, X. Dajaku, W. Xie, and D. Gerling, "Comparison of two different IPM traction machines with concentrated winding," *IEEE Trans. Ind. Electron.*, vol. 63, no. 7, Jul. 2016.

[11] Z. Q. Zhu, Z. P. Xia, L. J. Wu, and G. W. Jewell, "Influence of slot and pole number combination on radial force and vibration modes in fractional slot PM brushless machines having single- and double-layer windings," in *Proc. IEEE Energy Convers. Congr. Expo.*, San Jose, CA, 2009, pp. 3443–3450.

[12] D.-Y. Kim, M.-R. Park, J.-H. Sim, and J.-P. Hong, "Advanced method of selecting number of poles and slots for low-frequency vibration reduction of traction motor for elevator," *IEEE/ASME Trans. Mechatron.*, vol. 22, no. 4, pp. 1554–1562, Aug. 2017.

[13] M.-R. Park, D.-Y. Kim, J.-W. Jung, and J.-P. Hong, "Design of high torque density multi-core concentrated flux-type synchronous motors considering vibration characteristics," in *Proc. IEEE Int. Electric Mach. Drives Conf.*, Miami, FL, 2017, pp. 1–6.

[14] J. F. Gieras, C. Wang, and J. C. Lai, "Magnetic fields and radial forces in polyphase motors fed with sinusoidal currents," in *Noise of Polyphase Electric Motors*, 1st ed., Boca Raton: CRC Press, 2006, ch. 2, pp. 21–64.

[15] J.-W. Jung, S.-H. Lee, S.-H. Lee, J.-P. Hong, D.-H. Lee, and K.-N. Kim, "Reduction design of vibration and noise in IPMSM type integrated starter and generator for HEV," *IEEE Trans. Magn.*, vol. 46, no. 6, pp. 2454–2457, Jun. 2010.

[16] D. Y. Kim, J. K. Nam, and G. H. Jang, "Reduction of magnetically induced vibration of a spoke-type IPM motor using magnetomechanical coupled analysis and optimization," *IEEE Trans. Magn.*, vol. 49, no. 9, pp. 5097–5105, Sep. 2013.

[17] J.-P. Hong, K.-H. Ha, and J. Lee, "Stator pole and yoke design for vibration reduction of switched reluctance motor," *IEEE Trans. Magn.*, vol. 38, no. 2, pp. 929–932, Mar. 2002.

[18] S. Zuo, F. Lin, and X. Wu, "Noise analysis, calculation, and reduction of external rotor permanent-magnet synchronous motor," *IEEE Trans. Ind. Electron.*, vol. 62, no. 10, pp. 6204–6212, Oct. 2015.

[19] H.-S. Kim and B.-I. Kwon, "Optimal design of motor shape and magnetisation direction to obtain vibration reduction and average torque improvement in IPM BLDC motor," *IET Electr. Power Appl.*, vol. 11, no. 3, pp. 378–385, 2017.

[20] G.-Y. Zhou and J.-X. Shen, "Rotor notching for electromagnetic noise reduction of induction motors," *IEEE Trans. Ind. Appl.*, vol. 53, no. 4, pp. 3361–3370, Jul./Aug. 2017.

[21] M. Jafarboland and H. B. Farahabadi, "Optimum design of the stator parameters for noise and vibration reduction in BLDC motor," *IET Electr. Power Appl.*, vol. 12, no. 9, pp. 1297–1305, 2018.

[22] J.-W. Jung, D.-J. Kim, J.-P. Hong, G.-H. Lee, and S.-M. Jeon, "Experimental verification and effects of step skewed rotor type IPMSM on vibration and noise," *IEEE Trans. Magn.*, vol. 47, no. 10, pp. 3661–3664, Oct. 2011.

[23] C. Gan, J. Wu, M. Shen, S. Yang, Y. Hu, and W. Cao, "Investigation of skewing effects on the vibration reduction of three-phase switched reluctance motors," *IEEE Trans. Magn.*, vol. 51, no. 9, Sep. 2015, Art. no. 8203509.

[24] D.-J. Kim, J.-W. Jung, J.-P. Hong, K.-J. Kim, and C.-J. Park, "A study on the design process of noise reduction in induction motors," *IEEE Trans. Magn.*, vol. 48, no. 11, pp. 4638–4641, Nov. 2012.

[25] Y.-H. Jung, M.-S. Lim, M.-H. Yoon, J.-S. Jeong, and J.-P. Hong, "Torque ripple reduction of IPMSM applying asymmetric rotor shape under certain load condition," *IEEE Trans. Energy Convers.*, vol. 33, no. 1, pp. 333–340, Mar. 2018.

Young-Hoon Jung received the bachelor's degree in mechanical engineering from Hanyang University, Seoul, South Korea, in 2013. He is currently working toward the Ph.D. degree in automotive engineering with Hanyang University, Seoul, South Korea. His research interests are electric machine design for automotive and robot applications, and ultra-high speed motors.

Min-Ro Park received the bachelor's degree in electrical engineering from Chungnam National University, Daejeon, South Korea, in 2013. He is currently working toward the Ph.D. degree in automotive engineering with Hanyang University, Seoul, South Korea. His research interests are design and analysis of electric machine for electromechanical system.

Myung-Seop Lim (Member, IEEE) received the bachelor's degree in mechanical engineering from Hanyang University, Seoul, South Korea, in 2012, and the master's and Ph.D. degrees in automotive engineering from Hanyang University, Seoul, South Korea, in 2014 and 2017, respectively.

From 2017 to 2018, he was a Research Engineer with Hyundai Mobis, Yongin, South Korea. From 2018 to 2019, he was an Assistance Professor with Yeungnam University, Daegu, South Korea. Since 2019, he has been with Hanyang University, Seoul, South Korea, where he is currently an Assistant Professor. His research interests include electromagnetic field analysis and electric machinery for mechatronics systems such as automotive and robot applications.